Validation of a Suspension Model and its Elastic Behaviour Demonstrated at the Formula Student Race Car of the University Duisburg-Essen

*Frédéric Etienne Kracht**
Alex Armando Roempler Dellien
Dieter Schramm

Chair of Mechatronics
Department of Mechanical and Process Engineering,
Faculty of Engineering,
University of Duisburg-Essen,
47057 Duisburg, Germany
**kracht@mechatronik.uni-duisburg.de*

ABSTRACT

Various types of models have been used for many years to predict the motion of vehicle chassis. The complexity of these models ranges from rather basic to sophisticated models including the elasticity of selected components. For the latter flexible multibody models can be used to model in detail the elasto-kinematic behaviour of a vehicle suspension system by modelling components as FE bodies. However, a model can only be considered valid after a successful validation process. Standardized tests like the wheel travel test and the double-lane change manoeuvres are suitable for this purpose. It is not trivial to measure the kinematics due to the dynamic elastic deformations of the parts. This paper demonstrates how to assess the significance of such effects on the kinematics. Laser sensors are used to measure the time-dependent position of the parts. Stress gauges are also used to record stress and strain data of the metallic parts. Acceleration sensors are then applied to calculate the influence of the moving chassis. All measurements are taken from the double-wishbone suspension equipped formula student race car. For the validation of the models, experimentally measured data is compared against simulation data. Differences are minimized using optimization tools. Acceptable agreement between

ISSN 1823- 5514, eISSN 2550-164X
Received for review: 2017-10-11
Accepted for publication: 2018-06-20
Published: 2018-11-30

measured data and simulation data were obtained. The result is that non-measured manoeuvres can also be simulated using the validated model thereon after.

Keywords: Elasto-kinematic; formula-student; vehicle models; suspension; FEM

Introduction

To understand the motion of a vehicle in different situations, conditions and circumstances, an investigation of the vehicle dynamics is mandatory. Displacement, velocity, acceleration, varying forces, strain and stress in chassis parts among other characteristics are examples of what can be analyzed from dynamic tests on a vehicle. Over many years, scientists and automobile companies have invested tremendous amounts of research capacity not only in developing the vehicle components but also on how to get suitable measurements and properties of a vehicle's behaviour [1], [2]. However, tests on prototypes require expensive investments and are highly time-consuming. This has made software manufacturers enter this field and to develop better methods and procedures to investigate the vehicle's dynamics in less expensive, but faster and equally reliable ways.

Therefore, mathematical models of different types have been successfully used for many years. However, contemporary modelling techniques could not keep pace with the demand for even more complex and close-to-reality models, despite all progress in computer software and hardware. Depending on the application, models exist with sophisticated or straightforward approaches. On one hand, simple models result from the necessity for short computation times. Examples are optimization tasks with many iterations steps or even real-time applications. The requirement for optimization tasks with more parameters and quick system adjustments inappropriate time, demands efficient simulation models [3]. Real-time applications are normally performed by ECUs, with still existing limitations, as part of driving dynamics control systems. Therefore, classical active control systems in vehicles are in general oriented on basic mathematical models like the single track model of Rieckert and Schunck [4], these, however, have been proven to be sufficient for control systems as versatile as the Electronic-Stability-Program (ESP) and its variants. Due to the further development of driver assistance systems, such as the active chassis for roll stabilization, these models are required to deliver a higher accuracy.

On the other hand, there are very complex models that reflect the effects of elasticity. Among other uses, these are used for vehicle pre-development with respect to critical load limits or additional suspension systems research. The modelling of such multi-body systems with flexible bodies is time-

consuming and the computation time thereafter is very high. Furthermore, the entire FEM analysis must be simulated again when only one parameter, such as the length of a wishbone, is changed. However, even then the need to reduce development costs, which is associated with time, emerges.

In general, increased modelling accuracy gives results closer to the real system-behaviour, unfortunately always at the expenditure of extended computation time [4]. Therefore, the ideal model is a compromise between runtime and simulation accuracy determined by the actual application.

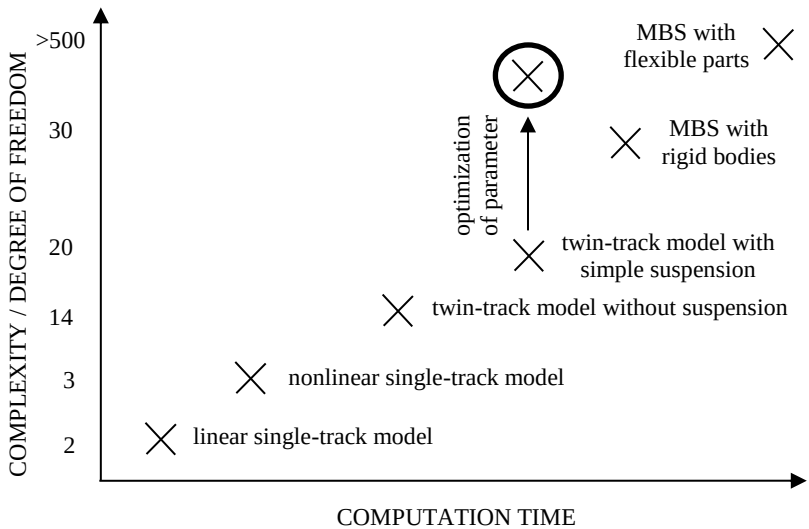

Figure 1. The relation between complexity and computation time of vehicle models

In the past, it has been successfully demonstrated that by optimizing bearing elasticities, the overall elasticity of a suspension can be modelled [5]. Hereby, the elastic properties of the bushings are modified in a way to reflect the structural elasticity of metallic components. It is thus possible to achieve the same model behaviour of complex models like multibody simulation models (MBS) by changing parameters of simpler models (see Figure 1). In other words, by parametrizing a simpler set of equations obtained from the simpler model, which has fewer degrees of freedom, the same accuracy can be obtained. To achieve this, an optimizer must be used as seen in Figure 2. The optimizer adjusts the parameters of the system up to the point that the error is less than a defined maximum. Since a great deal of data is required to optimize the parameters, it is a good idea to simulate them using a validated reference model. The validation should be carried out through relevant static and dy-

namic tests (see Figure 3). There are different sets of parameters for rigid bodies $\boldsymbol{p}_V$ and flexible bodies $\boldsymbol{p}_{V,\varepsilon}$. The output of the models are the acceleration $\ddot{\boldsymbol{r}}_V$ of the car and for the elastic model the stresses $\boldsymbol{\sigma}_V$ of the bodies, which are compared with the measured motion $\ddot{\boldsymbol{r}}^*_{V,\varepsilon}$ and measured stresses $\boldsymbol{\sigma}^*_V$. As a result, after the optimization of the parameters, the reference model is valid for every driving maneuver.

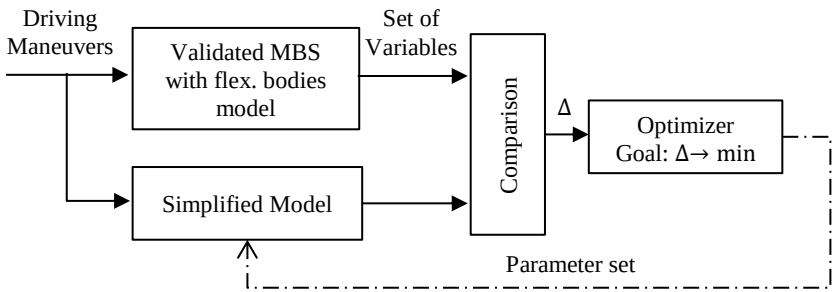

Figure 2. Parameter optimization with simulation data

No matter the level of accuracy a model has, a validation must be carried out successfully. It's shown in the past, that this is possible for different types of suspension systems [6]. In most cases the, travel of the spring-/damper-system is measured and with this, the kinematics are calculated [1]. The problem is that elasticities change the ideal kinematic movement and therefore a more precise technique must be used. In this paper, a combination of different sensor types is used. Optical displacement sensors, deformation sensors more specifically strain gauges and accelerometers are applied.

The scope of this paper is to build, model, validate and simulate a reference model with high complexity and elastic behaviour modelled car is the racing car of the Electric Formula Student team of the University of Duisburg-Essen. The aim is to analyze how the car responds to different tests with respect to the ISO norms. This is done using the software ADAMS (Automatic Dynamic Analysis of Mechanical Systems) offered by the MSC Software Company. The goal of the paper is to investigate how the racing car behaves on different tests.

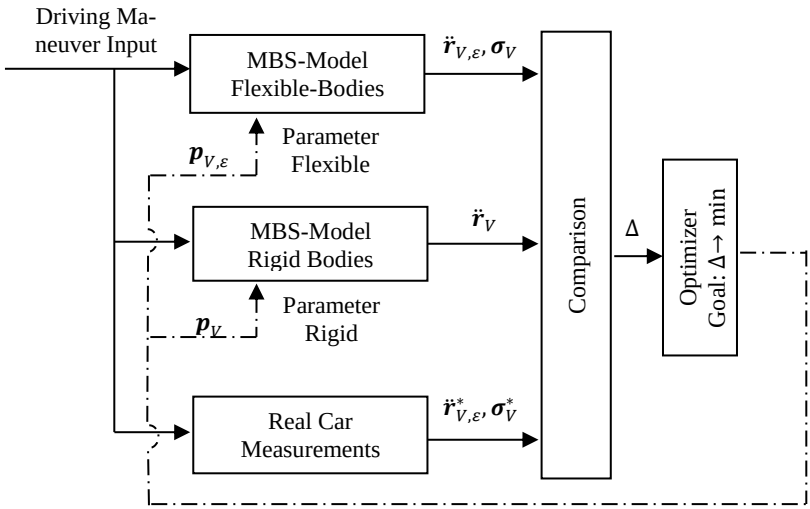

Figure 3. Validation process

This paper is structured into three main chapters: The chapter VEHICLE MODELS gives an overview on the racing car and the modelling of a multibody system on ADAMS. This chapter also illustrates the topology of a full vehicle and dividing it into subsystems as suspension, steering, powertrain and other subsystems, which are modelled on the software. In addition, the modelling of flexible bodies is explained. Within the chapter MEASUREMENTS, the sensors and how they were used is explained. Furthermore, it is shown how to calculate the kinematics and elasto-kinematics out of the measured data. Static tests and dynamic driving manoeuvres are used to cover both relevant domains. Within the chapter VALIDATION, the simulation data is compared with the measured data. The parameters of the model are adapted by appropriate techniques. To conclude, a summary is presented and the scope for future work is described.

Vehicle Models

Formula Student Race Car

The race car of the University of Duisburg-Essen named A40-02 took part in the competitions of the Formula Student Electric in the years 2015 and 2016 (see Figure 4). Formula Student is an international construction competition for students of different courses of studies.

The car weighs approximately 300 kg excluding the driver's weight. It is equipped with a double wishbone front suspension with two wishbone-

shaped arms to locate the wheels. The same suspension system is applied to the rear, however considering some additional parts such as the rocker arm and pushrod. A shock absorber consisting of the damper and the spring of a mountain bike supplied by the company ROCKSHOX with the model name VIVID R2C mounts to the wishbone, controlling the vertical movement of the racing car. The car is motorized with two electric motors of the type EMRAX 228 supplied by the company ENSTROJ. Both electric motors have a maximum total power of 100 KW. Moreover, the motor is powered by a 6 KWh 30C LiPo cell battery supplied by the KOKAM Company. [7] Instead of connecting the motors to a differential, they are connected to two planetary gearboxes having a transformation ratio of 4:1, which divides the rotating torque between the two wheels. This allows each wheel to rotate at a different speed.

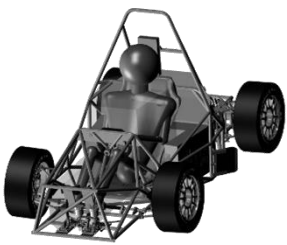

Figure 4. Formula Student Racecar A40-02

Reference Model: Multibody Model with Rigid Bodies

Multi-body Systems (MBS) consist of one or more rigid bodies, which are connected by springs, dampers and joints [4]. The massless force elements (e.g. springs, dampers, servomotors) are represented by applied forces. A four-wheeled vehicle according to its structure (body) and its four wheels consists of five single masses. By assuming each free moving part of a rigid body, it can be concluded that each has six degrees of freedom (three translational and three rotational). Therefore, considering the whole vehicle results in $5 \times 6 = 30$ degrees of freedom (in short, DoF). [8]

In the MBS analysis, one way is to describe the equations of motion using Newton's and Euler's equations and incorporating additional constraints resulting from joints by applying the principle of d'Alembert or Jourdain [4]. The dynamics of the MBS is thereby fully described via the kinematic differential equations and the equations of motion:

$$\dot{\boldsymbol{y}} = \boldsymbol{K}(\boldsymbol{y})\boldsymbol{z}, \tag{1}$$

$$\boldsymbol{M}(\boldsymbol{y})\dot{\boldsymbol{z}} = \boldsymbol{q}(\boldsymbol{y}, \boldsymbol{z}), \tag{2}$$

with the generalized coordinates $\boldsymbol{y}$ and the generalized velocities $\boldsymbol{z}$. The mass matrix $\boldsymbol{M}(\boldsymbol{y})$ represents the mass and inertial properties of the system whereas

the vector of the generalized forces and torques $\boldsymbol{q}(\boldsymbol{y},\boldsymbol{z})$ accounts for the applied forces [4].

The software used for the Multibody System of the race car is ADAMS/CAR. Templates in ADAMS/CAR define the main role and parameters of the subsystem. To build a template, the basic topology is to construct what is called "hard points", where each hard point in the template defines the location -but not the orientation- of a specific point on the CAD model. Despite the presence of a tremendous number of points on the model, only a few of them can be chosen as hard points for the template construction. Those points are mostly chosen to be at a place where joints are located or where the connection between two or more parts exists. Furthermore, those points can be chosen to be on the edge of a part or even at the centre of gravities of some parts.

After setting the hard points, the parts must be built. In ADAMS/CAR, parts are coordinate points containing important physical values, like the mass and the moments of inertia (I_{xx}, I_{yy}, I_{zz}). The parts are to be either assigned to a hard point location or centered between two hard points. In contrast to the hard points, the parts can be set at specific orientations as well as be assigned to a specific material (most commonly steel or aluminum).

Adding geometry to the part provides a shape for the required template. For example, an added link demonstrates a part that connects two points. To connect three points as one part, the arm geometry can be chosen. The geometry parameters automatically adjust the masses of the parts; therefore, it is important to set the mass and mass moment of inertia properties after inserting the parameters of the geometries. This means that a bigger diameter link leads to a larger mass. Connecting the parts together is done through the joints, which constrain the movement of the parts to a specific number of degrees of freedom. The geometrical representation makes it easier in the visualization of the template to see which parts are properly connected and where, as well as to show what are the types of joints used to connect the corresponding parts. One of the most important options in Adams/Car is adding the "mounts". Mounts are "imaginary" parts which are added to allow the communication between the subsystems, so if a front suspension subsystem is to be connected to the steering subsystem, Adams searches for mount parts on each subsystem and these contain the information at which specific points the subsystems are to be attached.

Finally, yet very important is the setting of parameters. Parameter variables are the values used for the analysis of the system, and for each newly added parameter an automatically communicator is created by Adams, which uses these values as well for the connection between subsystems. Figure 5 shows the main subsystems, which have to be assembled together to build and simulate the whole vehicle.

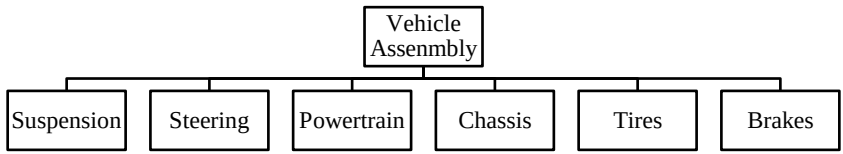

Figure 5. Vehicle main components

The extension of MBS with flexible bodies leads to a more complex model. The additional DoF due to elasticity can be represented by different methods like by deformable beams or as FE models. The single linear modes are determined by the Craig-Bampton reduction in modal analysis and then integrated as an elastic component [9]. Thus, the flexible MBS analysis is a suitable modelling method to analyze elasticities and resulting strains and stresses. In addition, the individual linear system modes are integrated. By reducing the modes, the DoF is reduced; however, still, a few hundred DoF remain.

Based on the scope of the investigation task a simulation model must be designed with a tradeoff between complexity and performance. It should be mentioned, that both, a set of standard MBS simulations and a FEM analysis is often needed. The overall goal is to simulate the system behaviour as precise as possible. The deformation of single parts within the system, however, contribute to a great extent to that behaviour and also provide high accuracy. Therefore both, deformation and dynamics must be considered in the model. The modelling method is therefore in general only suitable as a high accuracy reference model which is the base of an optimization of a simplified model.

The components listed in Table 1 were discretized using the software MSC Adams / ViewFlex. Starting from the generated network, the existing modes were determined within a modal analysis. In this case, no modes were deactivated in favour of accuracy.

Table 1 FEM component overview

Part	No. of elements	No. of nodes	No. of modes
Lower wishbone	9892	2743	39
Upper wishbone	3880	1172	315
Wheel carrier	15316	3968	224
Tie rod	1954	627	35

Measurement

Sensors

To validate the model, an experimental set-up consisting of seven laser sensors, four rosette strain gauges (layout: 0º,45º,90º, with temperature compensation) and two three-axis accelerometers were used. The data from the car's onboard ECU was also saved, which includes measurements for the steering wheel angle, acceleration, individual wheel angular velocities, etc. The Formula Student electric car's front right suspension of the E-Team from the University Duisburg Essen was mounted with a self-designed support rack to accommodate the 7 Laser Sensors. The rack was fixed to the chassis at 4 points and it did not inhibit the function or movement of the suspension system in any way.

Table 2 Sensor Hardware

Hardware Type	Brand	Model	Quantity	Characteristics
Laser Sensors	Sensopart Industrie-sensorik GmbH	FT 25 RA-170-PSU-M4M	7	– Measuring Range: 30 - 200 mm – Resolution: 0,68 mm – Measuring Freq.: up to 900 Hz – Light Type: Infrared LED – Operating Voltage: 13 - 30 V DC – Output signal: 1-10 V (Analog) max. 3 mA – Connection: M8 4-Pole
Voltage Dividers	Self-made	-	7	– Division ratio: 2:1 – Resistance precision: 1%
A/D Converters	Arduino	Mega 2560	2	– Microcontroller: ATmega2560 – 54 digital I/O pins – 16 Analog Inputs – 16 MHz crystal oscillator – USB interface
Strain Gauges	ME-Meßsysteme GmbH	C2A-06-062WW-350	4	– Strain Gauge Type: Rosette, stacked (0,45,90) – Resistance: 350 Ohm – Dimensions: 7.06 mm x 8.00 mm – Length of Grid: 1.52 mm – Temperature Compensation: Steel (10.8 ppm/ ℃)
Voltage Amplifiers	ME-Meßsysteme GmbH	GSV-4USB SUB D-37	3	– 4 Channel strain gauge Amplifier with USB Interface – SUB D-37 plug for Sensor connection – Analog input configurable 2mV/V , 10mV/V, 0-5V – Bridge completion for quarter Bridges – Measuring Freq.: up to 500 Hz – Dimensions: 120mm X 109mm X 35mm

Two gray polymer plates with a maximum residual ripple of less than 10% and a remission close to 18% (which were the reference surface conditions for the laser Sensor's calibration) were attached to the lower wishbone of the suspension and the wheel carrier as planar surfaces for the laser sensors to measure the kinematics of the suspension along its degrees of freedom. The laser Sensor's seven analogue output signals were converted to digital using first voltage dividers to adjust the voltage range for the Arduinos and then two Arduino Mega boards which acted as analogue/digital converters. Finally, the Arduino output in bits was saved on an onboard computer using a serial Terminal. Two rosette strain gauges were placed on the wheel carrier and the other two on the lower wishbone. The gauges were connected to dedicated voltage amplifiers forming a quarter Wheatstone bridge each and used to analyze the elasto-kinematics of the wheel carrier and lower wishbone by measuring the deformation of these parts in $\mu m/m$. The two three-axis accelerometers were located on the polymer plate attached to the wheel carrier and the other one attached to the sensor rack just above the upper wishbone of the suspension. The following table describes some of the specifics of the used hardware in Table 2.

Kinematic Measurement

Two Arduino boards were used to maintain the necessary data acquisition rate of 500 Hz. One Arduino board is used to convert the signals from four sensors and the other one for the other three. Time measurement is synchronized at the beginning between the two boards so that the time stamps of both can later be compared even though, each individual measurement happens at a slightly different time on each board due to the difference in the number of signals each board must handle. The Arduino Mega's analogue inputs have a resolution of 10 bits, which means a total of 1,024 different discretized values it can be set to, to describe a voltage between ground and usually 5 V. Therefore, at the output, we got a value in between 0 and 1,023. After calibration, the laser sensors deliver a linear relationship between distance and voltage in a range of 30 mm to 150 mm. The output is 1 V for 30 mm and 10 V for 150 mm. The Arduino boards can handle a voltage of maximum 5 V, therefore voltage dividers had to be designed to bring the output voltage of the laser sensors to a range in between 0.5 and 5 V (see Figure 6). This means that the output of the laser sensors has a range of 4.5 V. These values are discretized by the Arduino boards into 1024 possible values. Finally, the values in bits are then converted to distance using the following conversion formulas:

$$\text{Measurement [V]} = (\text{Measurement [Bits]}) \cdot \left(\frac{4.5}{1023}\right) \qquad (3)$$

$$\text{Measurement [mm]} = \left(\frac{(150-30)[\text{mm}]}{4.5\ [\text{V}]}\right) \cdot (\text{Measurement [V]}) - \left(\left(\frac{(150-30)[\text{mm}]}{4.5\ [\text{V}]}\right) \cdot 0.5\ [\text{V}]\right) + 30\ [\text{mm}]$$

The two sets of signals with their corresponding time stamps are brought together by interpolating one set into the timestamps of the other set using a cubic spline. This allows us to handle the sensor data at the same time stamps. Finally, the signal is passed through a low-pass filter to filter any possible noise or interference using 15 Hz as the cut-off frequency as signals with a higher frequency are not commonly found in the mechanical domain of suspension systems.

In order to measure the kinematic movement of the wheel suspension, it is necessary to determine first the number of degrees of freedom of the double-wishbone wheel suspension with the steering system. This kind of wheel suspension has, according to equation (4), two characteristic degrees of freedom. The isolated degrees of freedom are neglected.

$$\begin{aligned} \text{DoF} = & \underbrace{5 \cdot (6)}_{5\cdot\text{bodies}} - \underbrace{8 \cdot (6-3)}_{8\cdot\text{spherical joints}} - \underbrace{1 \cdot (6-5)}_{1\cdot\text{translatotional joint}} \\ = & \underbrace{1}_{\text{wheel vertical motion}} + \underbrace{1}_{\text{steering motion}} + \underbrace{3}_{\text{isolated DoF}} \end{aligned} \quad (4)$$

To assess the vertical and steering movement, two independent variables must be measured. In this case, the surfaces of the wheel carrier and the surface of the lower wishbone are to be measured.

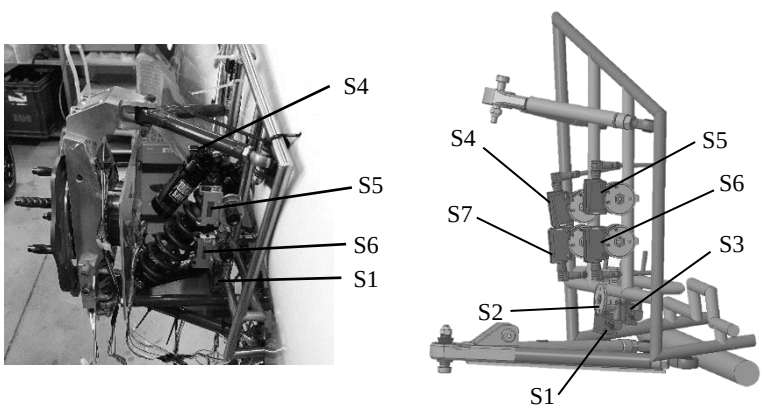

Figure 6. Rack and position of Laser sensors (Left: Actual, Right: CAD model)

By using at least three laser sensors, the distance to an attached plate is accurately measured. Since the position and the orientation of the laser sensors are known, this again results in a surface. In this case, four laser sensors are used for the wheel carrier and three for the lower wishbone. By measuring four points of a surface, possible measurement errors can be better compensated. Figure 7 shows the measurement of the lower wishbone. For a more precise measurement of the individual sensors positions, a reference point O_M is first used. Starting from a vehicle-fixed point on the sensor mount, vectors to the individual sensors are measured in the CAD files and, if necessary, corrected with tolerances in the real system. Furthermore, the transformation matrices ${}^{V}\boldsymbol{T}_{S}$ of the sensors coordinate system to the vehicle-fixed coordinate system are determined by the alignment of the sensor rack and the design-related rotational axis. The most sensitive coordinate system is hereby rotated in such a way that it is measured in the respective y-direction.

This results in the vectors for the description of the planar plate on the lower wishbone with the temporally variable measurements of the distances of the three sensors l_1, l_2 and l_3

$$ {}^{V}_{V}\boldsymbol{r}_{Pi}(t) = {}^{V}\boldsymbol{T}_{Si}\begin{pmatrix} 0 \\ l_i(t) \\ 0 \end{pmatrix} + {}^{V}_{M}\boldsymbol{r}_{Si} + {}^{V}_{V}\boldsymbol{r}_{M}, \quad i = 1,2,3 \qquad (5) $$

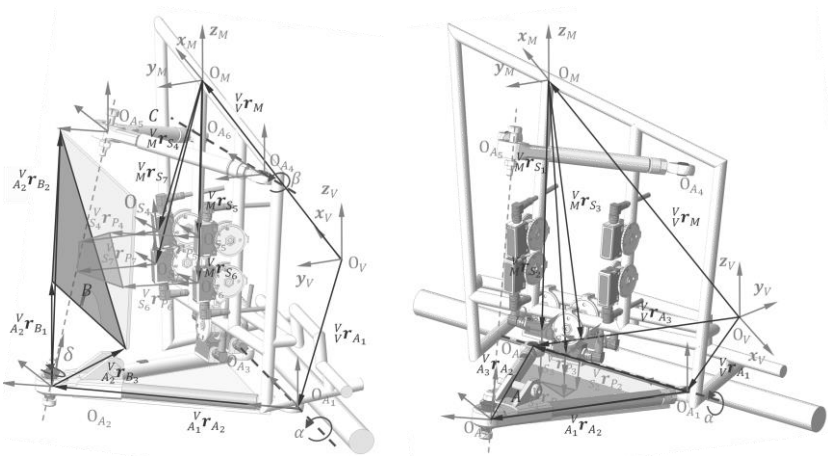

Figure 7. Upper wishbone and wheel carrier measurement

Using the three determined vectors ${}^{V}_{V}\boldsymbol{r}_{P1}(t)$, ${}^{V}_{V}\boldsymbol{r}_{P2}(t)$ and ${}^{V}_{V}\boldsymbol{r}_{P3}(t)$ from the sensor point P_1 two vectors span a surface. ${}^{V}\boldsymbol{T}_{S1/S2/S3}$ are the transformation matrices of the sensor orientation in the vehicle frame. The cross product thus results in a normal vector to the temporally moved surface

$$ {}^{V}\boldsymbol{n}_{P1,P2,P3}(t) = \frac{\left({}_{V}^{V}\boldsymbol{r}_{P3}(t) - {}_{V}^{V}\boldsymbol{r}_{P1}(t)\right) \times \left({}_{V}^{V}\boldsymbol{r}_{P2}(t) - {}_{V}^{V}\boldsymbol{r}_{P1}(t)\right)}{\left\| \left({}_{V}^{V}\boldsymbol{r}_{P3}(t) - {}_{V}^{V}\boldsymbol{r}_{P1}(t)\right) \times \left({}_{V}^{V}\boldsymbol{r}_{P2}(t) - {}_{V}^{V}\boldsymbol{r}_{P1}(t)\right) \right\|}. \quad (6) $$

In order to determine the minimalized coordinate of the DoF, the normal vector must now be determined which results from the rotational DoF of the lower wishbone

$$ {}^{V}\boldsymbol{n}_{A}(t) = \frac{({}_{V}^{V}\boldsymbol{r}_{A3} - {}_{V}^{V}\boldsymbol{r}_{A1}) \times ({}_{V}^{V}\boldsymbol{r}_{A2}(t) - {}_{V}^{V}\boldsymbol{r}_{A1})}{\| ({}_{V}^{V}\boldsymbol{r}_{A3} - {}_{V}^{V}\boldsymbol{r}_{A1}) \times ({}_{V}^{V}\boldsymbol{r}_{A2}(t) - {}_{V}^{V}\boldsymbol{r}_{A1}) \|}, \quad (7) $$

$$ \text{with } {}_{V}^{V}\boldsymbol{r}_{A2}(t) - {}_{V}^{V}\boldsymbol{r}_{A1} = {}^{V}\boldsymbol{T}_{A}(\alpha(t))\, {}_{A1}^{A}\boldsymbol{r}_{A2}. \quad (8) $$

${}_{V}^{V}\boldsymbol{r}_{A1/A2/A3}$ are the hardpoints of the lower wishbone. Since the normal vector of the measured plate ${}^{V}\boldsymbol{n}_{P1,P2,P3}(t)$ and the normal vector of the lower wishbone ${}^{V}\boldsymbol{n}_{A}(t)$ must be the same, (6), (7) and (8) follows in the implicit equation

$$ \frac{\left({}_{V}^{V}\boldsymbol{r}_{P3}(t) - {}_{V}^{V}\boldsymbol{r}_{P1}(t)\right) \times \left({}_{V}^{V}\boldsymbol{r}_{P2}(t) - {}_{V}^{V}\boldsymbol{r}_{P1}(t)\right)}{\left\| \left({}_{V}^{V}\boldsymbol{r}_{P3}(t) - {}_{V}^{V}\boldsymbol{r}_{P1}(t)\right) \times \left({}_{V}^{V}\boldsymbol{r}_{P2}(t) - {}_{V}^{V}\boldsymbol{r}_{P1}(t)\right) \right\|} = \frac{({}_{V}^{V}\boldsymbol{r}_{A3} - {}_{V}^{V}\boldsymbol{r}_{A1}) \times ({}^{V}\boldsymbol{T}_{A}(\alpha(t))\, {}_{A1}^{A}\boldsymbol{r}_{A2})}{\| ({}_{V}^{V}\boldsymbol{r}_{A3} - {}_{V}^{V}\boldsymbol{r}_{A1}) \times ({}^{V}\boldsymbol{T}_{A}(\alpha(t))\, {}_{A1}^{A}\boldsymbol{r}_{A2}) \|}, \quad (9) $$

which must be solved for α using an iterative method. Because of inaccuracies in position, there is no clear solution. However, the error for this over-determined and nonlinear equation system (9) can be minimized by means of the least-squares non-linear curve adjustments. The following minimization problem is solved using the Levenberg-Marquardt algorithm:

$$ \left\| {}^{V}\dot{\boldsymbol{n}}_{A}(\alpha(t)) s_k + {}^{V}\boldsymbol{n}_{A}(\alpha(t)) \right\|_2^2 + \mu^2 \|\boldsymbol{s}_k\|_2^2 \rightarrow \min \quad \text{with } \mu > 0 \quad (10) $$

Here, $\boldsymbol{s}_k$ is the correction vector, and μ is the damping parameter, which can be freely choosen [10].

In order to determine the second DoF, the steering angle δ, the normal vector of the plate on the wheel carrier must now be determined (see Figure 7). The measurements of the sensors 4 to 7 are obtained

$$ {}_{V}^{V}\boldsymbol{r}_{Pi}(t) = {}^{V}\boldsymbol{T}_{Si} \begin{pmatrix} 0 \\ l_i(t) \\ 0 \end{pmatrix} + {}_{M}^{V}\boldsymbol{r}_{Si} + {}_{V}^{V}\boldsymbol{r}_{M}, \;\; i = 4, \ldots, 7. \quad (11) $$

Only three vectors are required to determine the normal vector. The fourth vector is for redundancy only. Beginning with the sensor point P_4 on the plate at the wheel carrier, two vectors on the plate's surface are formed using the other three vectors ${}_{V}^{V}\boldsymbol{r}_{P4}(t)$, ${}_{V}^{V}\boldsymbol{r}_{P5}(t)$ and ${}_{V}^{V}\boldsymbol{r}_{P6}(t)$ formed from each sensor

to its corresponding measured point on the plate $P_{4,5,6}$. The cross product thus results in a normal vector to the temporally moved surface.

$$ {}^{V}\boldsymbol{n}_{P4,P5,P6}(t) = \frac{\left({}_{V}^{V}\boldsymbol{r}_{P6}(t) - {}_{V}^{V}\boldsymbol{r}_{P4}(t)\right) \times \left({}_{V}^{V}\boldsymbol{r}_{P5}(t) - {}_{V}^{V}\boldsymbol{r}_{P4}(t)\right)}{\left\| \left({}_{V}^{V}\boldsymbol{r}_{P6}(t) - {}_{V}^{V}\boldsymbol{r}_{P4}(t)\right) \times \left({}_{V}^{V}\boldsymbol{r}_{P5}(t) - {}_{V}^{V}\boldsymbol{r}_{P4}(t)\right) \right\|}. \quad (12) $$

To determine the axis of rotation ${}_{A2}^{V}\boldsymbol{r}_{A5}$, the point A_5 must be determined. This results from the constraint that the distance between the point A_2 and A_5 is constant.

$$ \begin{aligned} \text{const.} &= \left\| {}_{V}^{V}\boldsymbol{r}_{A5} - {}_{V}^{V}\boldsymbol{r}_{A2} \right\| \\ &= \left\| {}^{V}\boldsymbol{T}_{C}(\beta(t))\left({}_{A4}^{C}\boldsymbol{r}_{A5}\right) + {}_{V}^{V}\boldsymbol{r}_{A5}(t) - {}_{V}^{V}\boldsymbol{r}_{A2}(t) \right\|. \end{aligned} \quad (13) $$

The vectors of the wheel carrier are determined as follows

$$ {}_{V}^{V}\boldsymbol{r}_{Bi}(t) = {}^{V}\boldsymbol{T}_{B}(\delta(t))\,{}_{A2}^{B}\boldsymbol{r}_{Bi} + {}_{V}^{V}\boldsymbol{r}_{A2}(t), \quad i = 1,2,3. \quad (14) $$

The normal vector of the wheel carrier results

$$ {}^{V}\boldsymbol{n}_{B}(t) = \frac{\left({}_{V}^{V}\boldsymbol{r}_{B3}(t) - {}_{V}^{V}\boldsymbol{r}_{B1}(t)\right) \times \left({}_{V}^{V}\boldsymbol{r}_{B2}(t) - {}_{V}^{V}\boldsymbol{r}_{B1}(t)\right)}{\left\| \left({}_{V}^{V}\boldsymbol{r}_{B3}(t) - {}_{V}^{V}\boldsymbol{r}_{B1}(t)\right) \times \left({}_{V}^{V}\boldsymbol{r}_{B2}(t) - {}_{V}^{V}\boldsymbol{r}_{B1}(t)\right) \right\|}. \quad (15) $$

Using equations (6), (7) and (8) the normal vector of the measured plate ${}^{V}\boldsymbol{n}_{P4,P5,P6}(t)$ and the normal vector of the wheel carrier have to be set to be parallel and yield the following equation

$$ \begin{aligned} &\frac{\left({}_{V}^{V}\boldsymbol{r}_{P6}(t) - {}_{V}^{V}\boldsymbol{r}_{P4}(t)\right) \times \left({}_{V}^{V}\boldsymbol{r}_{P5}(t) - {}_{V}^{V}\boldsymbol{r}_{P4}(t)\right)}{\left| \left({}_{V}^{V}\boldsymbol{r}_{P6}(t) - {}_{V}^{V}\boldsymbol{r}_{P4}(t)\right) \times \left({}_{V}^{V}\boldsymbol{r}_{P5}(t) - {}_{V}^{V}\boldsymbol{r}_{P4}(t)\right) \right|} \\ &= \frac{\left({}_{V}^{V}\boldsymbol{r}_{B3}(t) - {}_{V}^{V}\boldsymbol{r}_{B1}(t)\right) \times \left({}_{V}^{V}\boldsymbol{r}_{B2}(t) - {}_{V}^{V}\boldsymbol{r}_{B1}(t)\right)}{\left\| \left({}_{V}^{V}\boldsymbol{r}_{B3}(t) - {}_{V}^{V}\boldsymbol{r}_{B1}(t)\right) \times \left({}_{V}^{V}\boldsymbol{r}_{B2}(t) - {}_{V}^{V}\boldsymbol{r}_{B1}(t)\right) \right\|}. \end{aligned} \quad (16) $$

This, in turn, can be used to calculate the steering angle δ by means of an iterative solution method.

After solving the equation system, the characteristic parameters of suspension can be obtained according to their definitions

$$ \text{kingpin angle: } \sigma = \arctan\left(\frac{{}_{V}^{V}\boldsymbol{r}_{A5,y}(t) - {}_{V}^{V}\boldsymbol{r}_{A2,y}(t)}{{}_{V}^{V}\boldsymbol{r}_{A5,z}(t) - {}_{V}^{V}\boldsymbol{r}_{A2,z}(t)}\right), \quad (17) $$

$$ \text{caster angle: } \tau = \arctan\left(\frac{{}_{V}^{V}\boldsymbol{r}_{A5,x}(t) - {}_{V}^{V}\boldsymbol{r}_{A2,x}(t)}{{}_{V}^{V}\boldsymbol{r}_{A5,z}(t) - {}_{V}^{V}\boldsymbol{r}_{A2,z}(t)}\right). \quad (18) $$

The kingpin angle σ is measured in the yz-plane between the steering axis and normal vector to the road surface. It is defined positive when the top of the axis is closer to the vehicle center than the bottom of the axis. The kingpin influences the steering's self-aligning properties. The caster-angle σ is

measured in the xz-plane between the kingpin's axis and the normal vector of the road surface. The caster-angle is defined as positive if the projection of the bottom of the steering axis on the xy-plane is further forward on the x-direction than the top. [4]

Elasto-Kinetic Measurement

Two of the strain gauges are placed on the wheel carrier, which is made from Aluminium, and the other two on the lower wishbone which is made from Steel (see Figure 8).

Figure 8. Strain gauge position (Left: Actual, Right: CAD Model)

Therefore, two different temperature correction coefficients are necessary. The strain gauges used here are 350 Ω stacked rosette strain gauges with the configuration (0º, 45º, 90º). This means that three strain measurements from each gauge are measured. The total 12 channels of the four strain gauges are connected to three four-channel voltage amplifiers in a quarter Wheatstone bridge set-up. The voltage amplifiers had to be internally modified according to the chosen resistance which was 350 Ω, equal to that of the gauges. The measurements were then acquired through a program from the manufacturers of the voltage amplifiers called GSV-Multichannel v1.335. The rate of acquisition was set by the voltage amplifiers to 500 Hz. The measurements were then filtered with a low-pass filter and a cut-off frequency of 15 Hz.

Table 3 Principal angle calculation

y	$y \geq 0$	$y > 0$	$y \leq 0$	$y < 0$
x	$x > 0$	$x \leq 0$	$x < 0$	$x \geq 0$
Principal direction	$\phi = \frac{1}{2}(0° + \lvert\psi\rvert)$	$\phi = \frac{1}{2}(180° - \lvert\psi\rvert)$	$\phi = \frac{1}{2}(180° + \lvert\psi\rvert)$	$\phi = \frac{1}{2}(360° - \lvert\psi\rvert)$

Finally, the set of three measurements of each strain gauge was converted into principal stresses $\sigma_{1,2}$ and direction ϕ on the part through the following equations [11]

$$\sigma_{1,2} = \frac{E}{1-\nu} \cdot \frac{\epsilon_a + \epsilon_c}{2} \pm \frac{E}{\sqrt{2}(1+\nu)} \cdot \sqrt{(\epsilon_a - \epsilon_b)^2 + (\epsilon_c - \epsilon_b)^2}, \quad (19)$$

$$\tan(\psi) = \frac{2\epsilon_b - \epsilon_a - \epsilon_c}{\epsilon_a - \epsilon_c} = \frac{y}{x}, \quad (20)$$

$$\sigma_{\text{avg}} = \frac{1}{2}(\sigma_1 + \sigma_2), \quad (21)$$

where the following cases are used to determine the principal direction in Table 3.

Validation

Laser Sensor Calibration

Due to the deviation of the exact position and orientation of the sensors, a calibration is necessary. For this, the first test was to measure the distances of the laser sensors while the lower wishbone was set to an angle of $\alpha = 0°$. This is used to calculate a vector of the standard deviations s of all the data from the different sensors:

$$s = (0.0639 \quad 0.0499 \quad 0.0616 \quad 0.0868 \quad 0.0470 \quad 0.0398 \quad 0.0422)^T \text{ mm}. \quad (22)$$

With this the arithmetic mean S_{cal} is:

$$S_{cal} = \frac{1}{N}\sum_{i=1}^{N} S = (26.2688 \quad 32.3930 \quad 32.4671 \quad 64.4808 \quad 63.4469 \quad 70.8654 \quad 66.3923)^T \quad (23)$$

N is the scalar data set size which is in this case 9,207. S is the sensor data set of sensors S_1 to S_7.
The normal vector of the lower wishbone is in this case for the given α

$${}^V\boldsymbol{n}_{A,cal} = \frac{({}^V_V\boldsymbol{r}_{A3} - {}^V_V\boldsymbol{r}_{A1}) \times ({}^V\boldsymbol{T}_A(\alpha = 0)\,{}^A_{A1}\boldsymbol{r}_{A2})}{\|({}^V_V\boldsymbol{r}_{A3} - {}^V_V\boldsymbol{r}_{A1}) \times ({}^V\boldsymbol{T}_A(\alpha = 0)\,{}^A_{A1}\boldsymbol{r}_{A2})\|}. \quad (24)$$

To find the exact position and orientation of the sensor a minimum of the unconstrained multivariable function must be found. The main function of the sensors is, firstly, that the measured points build a surface, which has the same normal vector than the actual lower wishbone ${}^V\boldsymbol{n}_{A,cal}$ and secondly, the measured height of the plate z_A must be satisfied:

$$\left\| \frac{\left({}^{V}_{V}\boldsymbol{r}_{P3,\mathrm{cal}} - {}^{V}_{V}\boldsymbol{r}_{P1,\mathrm{cal}}\right) \times \left({}^{V}_{V}\boldsymbol{r}_{P2,\mathrm{cal}} - {}^{V}_{V}\boldsymbol{r}_{P1,\mathrm{cal}}\right)}{\left|\left({}^{V}_{V}\boldsymbol{r}_{P3,\mathrm{cal}} - {}^{V}_{V}\boldsymbol{r}_{P1,\mathrm{cal}}\right) \times \left({}^{V}_{V}\boldsymbol{r}_{P2,\mathrm{cal}} - {}^{V}_{V}\boldsymbol{r}_{P1,\mathrm{cal}}\right)\right|} - {}^{V}\boldsymbol{n}_{A,cal} \right\| \to 0, \qquad (25)$$

$$\text{and} \left\| \begin{pmatrix} \frac{{}^{V}_{S1}\boldsymbol{r}_{P1,z}}{\left|{}^{V}_{S1}\boldsymbol{r}_{P1}\right|} l_{1,\mathrm{cal}} + {}^{V}_{V}\boldsymbol{r}_{S1,\mathrm{z,cal}} \\ \frac{{}^{V}_{S2}\boldsymbol{r}_{P2,z}}{\left|{}^{V}_{S2}\boldsymbol{r}_{P2}\right|} l_{2,\mathrm{cal}} + {}^{V}_{V}\boldsymbol{r}_{S2,\mathrm{z,cal}} \\ \frac{{}^{V}_{S3}\boldsymbol{r}_{P3,z}}{\left|{}^{V}_{S3}\boldsymbol{r}_{P3}\right|} l_{3,\mathrm{cal}} + {}^{V}_{V}\boldsymbol{r}_{S3,\mathrm{z,cal}} \end{pmatrix} - \begin{pmatrix} z_A \\ z_A \\ z_A \end{pmatrix} \right\| \to 0, \qquad (26)$$

$$\text{with } {}^{V}_{V}\boldsymbol{r}_{Pi,\mathrm{cal}} = \frac{{}^{V}_{Si}\boldsymbol{r}_{Pi}}{\left|{}^{V}_{Si}\boldsymbol{r}_{Pi}\right|} l_{i,\mathrm{cal}} + {}^{V}_{V}\boldsymbol{r}_{Si,\mathrm{cal}}, \quad i = 1,2,3 \qquad (27)$$

The optimization algorithm used is a simple search method, the Nelder-Mead simplex algorithm [12]. With this, a good result for the laser sensor's position and orientation is found. The results of equation (25) and (26) improved from a value of 31.2700 to $2.9839 \cdot 10^{-5}$.

By using equations (13) to (15) with the calculation of ${}^{V}_{V}\boldsymbol{r}_{A2}(t)$ by equation (8) with $\alpha = 0°$ the normal vector ${}^{V}\boldsymbol{n}_{B}(\alpha = 0°)$ is calculated.

Similar to the optimization in (25) to (27) the position and orientation of the four other laser sensors S_4 to S_6 are found by using the same optimization algorithm.

$$\left\| \frac{\left({}^{V}_{V}\boldsymbol{r}_{P6,\mathrm{cal}} - {}^{V}_{V}\boldsymbol{r}_{P4,\mathrm{cal}}\right) \times \left({}^{V}_{V}\boldsymbol{r}_{P5,\mathrm{cal}} - {}^{V}_{V}\boldsymbol{r}_{P4,\mathrm{cal}}\right)}{\left|\left({}^{V}_{V}\boldsymbol{r}_{P6,\mathrm{cal}} - {}^{V}_{V}\boldsymbol{r}_{P4,\mathrm{cal}}\right) \times \left({}^{V}_{V}\boldsymbol{r}_{P5,\mathrm{cal}} - {}^{V}_{V}\boldsymbol{r}_{P4,\mathrm{cal}}\right)\right|} - {}^{V}\boldsymbol{n}_{B,cal} \right\| \to 0, \qquad (28)$$

$$\text{with } {}^{V}_{V}\boldsymbol{r}_{Pi,\mathrm{cal}} = \frac{{}^{V}_{Si}\boldsymbol{r}_{Pi}}{\left|{}^{V}_{Si}\boldsymbol{r}_{Pi}\right|} l_{i,\mathrm{cal}} + {}^{V}_{V}\boldsymbol{r}_{Si,\mathrm{cal}}, \quad i = 4,5,6. \qquad (29)$$

The improvement is reflected by the results of equation (28), which range from 0.1444 to $1.6320 \cdot 10^{-7}$. With this, all laser sensors are calibrated in the testing area.

Test Manoeuvre

Three standard tests are used for the study of the wheel suspension. On one hand, the static tests of wheel travel and the steering are performed [4]. These static tests represent the ideal characteristics of the wheel suspension and reflect the static influence on the elastic deformation.

On the other hand, a standard dynamic test, the double lane change is used, the ISO 3888-2 [13]. This test is used to analyze the dynamic behaviour

of the car. The wheel travel test involves the parallel displacement of the right and left wheel suspensions. With this, there is also a displacement of the centre of the wheels. The wheel position is defined by a set of parameters, which depend on the construction of the suspension system. The displacement of the centre of tire contact with the ground with respect to the vehicle-fixed reference frame is the wheel travel. The measurement starts from the neutral position and is positive during the suspension compression and negative during suspension extension. Within the steering test, the front wheels are deflected to the left and right limits.

The dynamic test is the ISO 3888-2, which evaluates the driving behaviour of the race car in the closed control loop. The test consists of an evasive manoeuvre with the subsequent deflection to the right lane. The total length of the test track is 61 m. The track width depends on the width of the race car which is 1.23394 m. Figure 9 shows the complete dimensions of the track for this special race car.

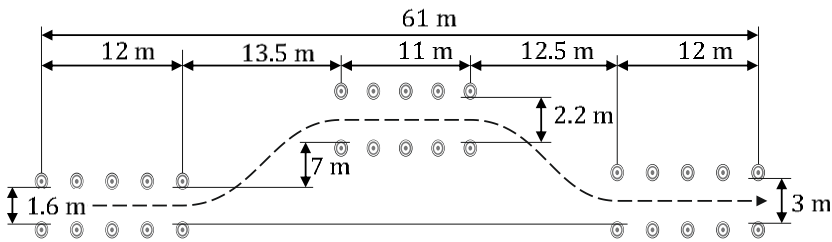

Figure 9. Double lane change according to ISO 3888-2 [13]

Test Results

Filters are used for all measurements to cancel measurement noise in the high-frequency domain. This Zero-phase digital filters use the Butterworth Lowpass filter design [14]. Figure 10 shows the caster angle and kingpin angle over the steering angle. Out of the measurement, two optimization functions are built. The first one optimizes the two hardpoints A_2 and A_5 so that the difference by 0° is zero. The second function includes that the caster angle and kingpin are relative constant by changing the steering angle with a little slope of the function. This hardpoints are implemented in ADAMS/CAR. The same optimization algorithm for the hardpoints by Nelder-Mead was used for the steering test and only after the third iteration the relative error was significantly reduced and high correlation between both data sets, the measured and the simulated where achieved as seen on Figure 10.

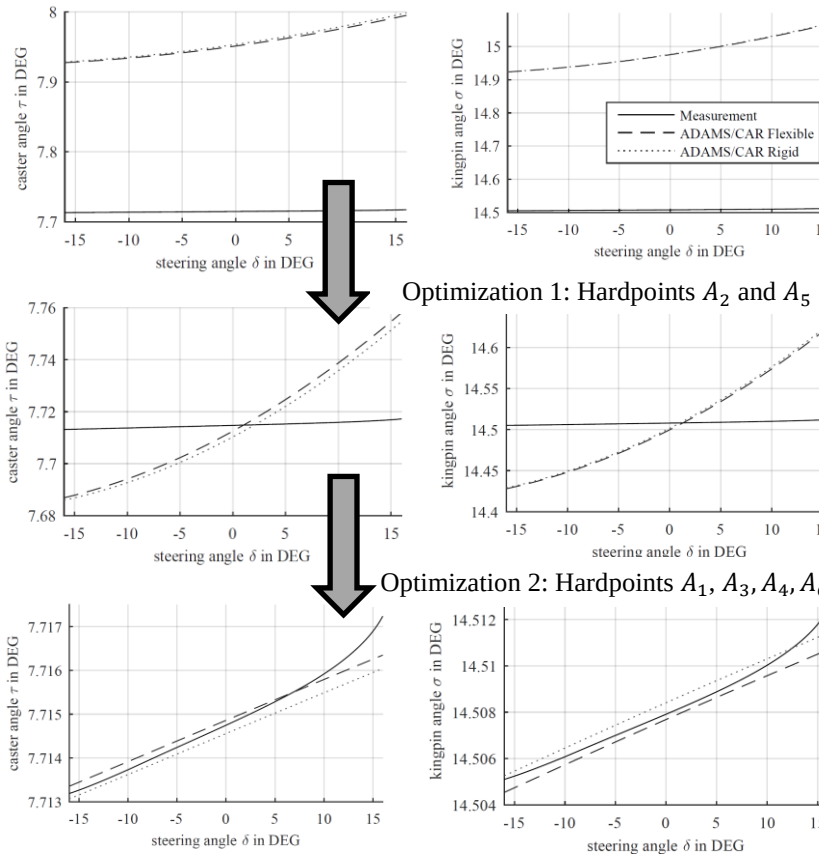

Figure 10. Steering Test – caster angle and kingpin angel – optimization steps ADAMS/CAR

Afterwards, the FEM analysis takes part. Here no optimization for parameters takes place. This is planned as a next step in the future work. In the model, the nodes at the measurement position of the real sensors are evaluated. Figure 11 shows the results of the stress analysis. The results differ significantly in the form but the magnitude of the values is similar. In the future, an optimization of the Young's modulus for the FEM Bodies of the parts needs to be performed. Hereby the problem is, that for each iteration a new mode analysis must take place. An optimization algorithm like the Nelder-mead simplex algorithm should be used to bring the data acquisition errors down and see an even better correlation between the simulation and the measured values as seen with the optimized parameters.

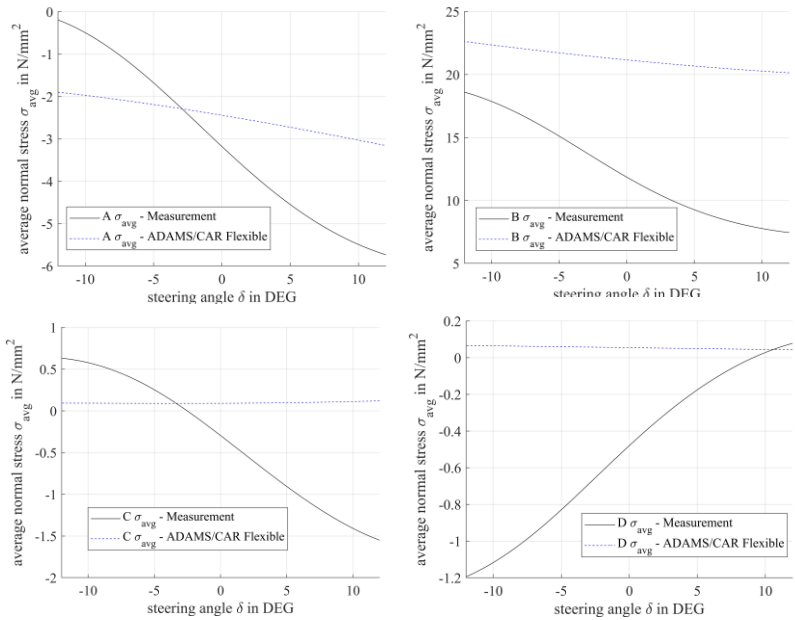

Figure 11. Steering Test – average normal stress

The wheel travel test results for the FEM analysis are shown next, here the initially calibrated points for the test correlate highly with the simulation, but in order to reduce the error, an optimization including the endpoints and possible middle points should be performed (see Figure 12 and Figure 13).

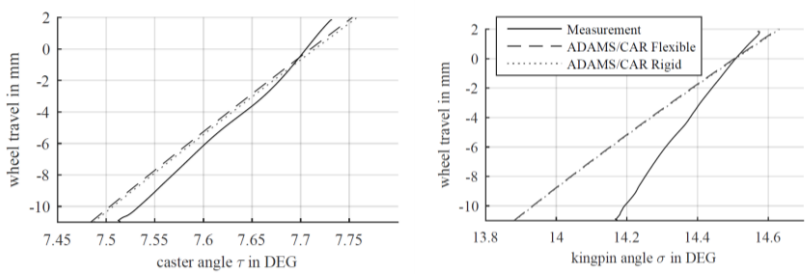

Figure 12. Wheel Travel – caster angle and kingpin angel

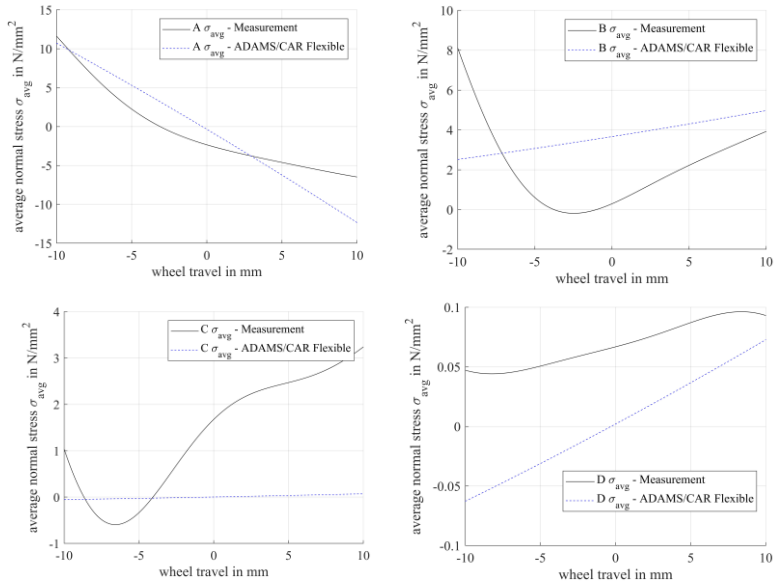

Figure 13. Wheel Travel Test – average normal stress

The dynamic double lane change test according to the ISO norm had an additional dataset, which was that of the accelerometers. This had to account for possible relative accelerations between the components and subsystems. Together with the optimization of the hardpoints, this delivers accurate results (see Figure 14). Minor deviations result from the driver's influence, cause it is an open-loop test.

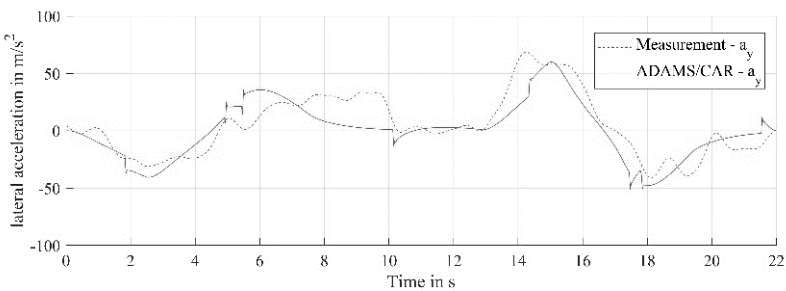

Figure 14. ISO Lane Change acceleration at the wheel carrier

Conclusion and Future Work

The advantages of using an MBS model with elastic properties have been shown. Most importantly the complexity of the model has been reduced through the optimization process of the parameters so that a relatively highly precise model that at the same time has faster computation times as other models with similar complexity results. The right front suspension of the Formula Student Electric vehicle of the University Duisburg-Essen has been modelled using the methods described in this paper and then the model has been validated through a process of comparison with actually acquired data from static and dynamic tests on the same vehicle.

The data acquisition methods during the tests have also been specifically designed for this purpose to provide relevant data. The data is then prepared accordingly and used to validate the model to a great extent. To have a more robust validation, and to provide an extension of the validation according to the modelling and optimization methods described in this paper, future work and testing have to be done. More specifically, the optimization must be extended by including more points as mentioned in the results and a similar optimization method should be used on the stress analysis. The results could be also used for the design optimization of race cars in the future to improve the performance and the handling.

References

[1] M.-C. O. Popescu and N. E. Mastorakis, "Testing and simulation of a motor vehicle suspension," International Journal Of Systems Applications, Engineering & Development, 3 (2) 74-83, (2009).

[2] J. Iwaniec, "Identification of car suspension system parameters on the basis of exploitational measurements," Diagnostyka. 14 (2013).

[3] M. Unterreiner, "Modellbildung und Simulation von Fahrzeugmodellen unterschiedlicher Komplexität," Universität Duisburg-Essen, Fakultät für Ingenieurwissenschaften» (Maschinenbau und Verfahrenstechnik, 2014).

[4] D. Schramm, M. Hiller, and R. Bardini, Vehicle Dynamics: Modeling and Simulation. Berlin, Heidelberg: (Springer Verlag 2014) pp. 405.

[5] F. E. Kracht, Y. Zhao, I. D. Schramm, and I. B. Hesse, "Development of a chassis model including elastic behavior for real-time applications," in 6th International Munich Chassis Symposium 2015. (Springer 2015) pp. 257-281.

[6] E. Wendeberg, "Using optimization to auto-correlate suspension characteristics to K&C measurements," Energy & Fuels, 24 (6) 3510-3516 (2010).

[7] D.-E. E-Team. (2016, 26.04.2017). Formula Student Electric at the Uni-

versity of Duisburg-Essen. Available: http://eteam-due.de/content/rennwagen-a40-02/
[8] M. Meywerk, Vehicle Dynamics. (John Wiley & Sons, 2015).
[9] R. Schwertassek and O. Wallrapp, Dynamik flexibler Mehrkörpersysteme: Methoden der Mechanik zum rechnergestützten Entwurf und zur Analyse mechatronischer Systeme Vieweg+Teubner Verlag, p. 476 (2014).
[10] K. Levenberg, "A method for the solution of certain non-linear problems in least squares," Quarterly of Applied Mathematics, 2 (2) 164-168 (1944).
[11] ME-Meßsysteme. (2017, May). Zweiachsiger Spannungszustand. Available: https://www.me-systeme.de/de/support/grundlagen/dms-grundlagen/spannungsanalyse-mit-dehnungsmessstreifen
[12] J. C. Lagarias, J. A. Reeds, M. H. Wright, and P. E. Wright, "Convergence properties of the Nelder--Mead simplex method in low dimensions," SIAM Journal on Optimization, 9 (1) 112-147 (1998).
[13] Passenger cars - Test track for a severe lane-change manoeuvre, 2002.
[14] V. O. Alan, W. S. Ronald, and R. John, "Discrete-time signal processing," New Jersey, Printice Hall Inc., (1989).